# Optimized EfficientNet for Detection of Endometrial Cancer Using Histopathological Images

**B. T. Keerthishree**
Department of Computer Science and Engineering, Adichunchanagiri Institute of Technology, Chikkamagaluru, Visvesvaraya Technological University, Karnataka, Belagavi, India
keerthishreebt@aitckm.in (corresponding author)

**Pushpa Ravikumar**
Department of Computer Science and Engineering, Adichunchanagiri Institute of Technology, Chikkamagaluru, Visvesvaraya Technological University, Karnataka, Belagavi, India
pushparavikumar@aitckm.in

*Received: 18 August 2025 | Revised: 12 September 2025, 24 October 2025, and 24 November 2025 | Accepted: 26 November 2025*

 *DOI: https://doi.org/10.48084/etasr.13925*

## ABSTRACT

**The diagnosis of endometrial cancer is highly dependent on histopathological analysis, which is often time-consuming and subjective. This study introduces an optimized EfficientNet-B7.5DeltaR model for the automatic detection of stromal tissue, blood vessels, and neutrophils in tissue patches. The novelty of this work lies in the extension of compound scaling with a new $\delta$-regularization factor and a widthwise convolution layer, enhancing generalization and reducing overfitting compared to the baseline EfficientNet. The proposed model was trained on 91 H&E-stained whole-slide images of endometrial carcinoma Pipelle biopsies from the Radboud University Medical Center, The Netherlands, and evaluated using standard classification and regression metrics. Results demonstrate a 6% improvement in validation accuracy, a 12% gain in $R^2$ score, and a 5% increase in F1-score over the baseline, confirming the improved generalization of the model for histopathological cancer analysis.**

***Keywords-EfficientNet; endometrial cancer; histopathological images; stroma; blood vessel; tumor***

## I. INTRODUCTION

Endometrial Cancer (EC), the most prevalent gynecological malignancy, demands accurate histopathological assessment for diagnosis and prognosis. However, manual analysis is laborious and prone to variability. With the rise of digital pathology and deep learning, automated image analysis offers improved accuracy and efficiency. EC tissue comprises stroma, blood vessels, and neutrophils—key components that influence tumor growth, angiogenesis, and inflammation. Precise segmentation and classification of these elements are essential for understanding tumor–microenvironment interactions and guiding the prediction of outcomes.

Deep learning has been widely applied to cancer image analysis, with EfficientNet demonstrating strong accuracy and efficiency for multi-cancer and skin disease classification [1, 2]. Multi-resolution and generalized deep learning frameworks have allowed endometrial cancer subtype prediction and scalable Whole-Slide Image (WSI) segmentation [3, 4]. Biological and stromal studies have provided critical insights into immune cell dynamics and tumor microenvironment characterization, supporting automated immunohistochemical analysis using deep learning [5, 6]. EfficientNet-based medical image classification has highlighted performance–efficiency trade-offs in skin cancer detection [7], while immunotherapy-focused studies emphasized the importance of mismatch repair status and tumor microenvironment in endometrial cancer [8]. Recent reviews summarized advances in machine learning and explainable AI for histopathological image analysis and lung cancer staging [9, 10]. Foundational architectures, such as EfficientNet, EfficientNetV2, Vision Transformers, ResNet, and Inception-ResNet, have shaped modern medical imaging models [11-16], with fastai facilitating rapid experimentation [17]. Clinical and imaging-based studies advanced endometrial cancer management, cytopathological analysis, and MRI-based invasion detection [18-20], while automated epithelial–stromal annotation improved WSI interpretation [21]. The spatial organization of tumor-stroma was shown to influence immunotherapy efficacy [22], and advanced segmentation networks have supported the delineation of the uterine region for treatment planning [23]. Broader surveys reviewed the role of artificial intelligence in cancer imaging [24], while recent works demonstrated deep learning-based microsatellite instability assessment, metastatic cancer detection, and large-scale WSI benchmarking using public datasets [25-27].

## II. MATERIALS AND METHODS

The dataset used in this study includes 91 H&E-stained Whole-Slide Images (WSIs) of endometrial carcinoma Pipelle biopsies, collected from Radboud University Medical Center, The Netherlands [27]. Originally scanned with a 3DHistech P1000 scanner at 0.25 µm/pixel and stored in MRXS format, the images were converted to TIFF at 0.5 µm/pixel for improved accessibility and compatibility with standard image analysis libraries. The dataset is released under the CC BY-NC 4.0 license for non-commercial research and educational use, without patient identifiers.

This study presents an optimized EfficientNet-B7.5ΔR model, introducing $\delta$-regularization and widthwise convolution to extend compound scaling.

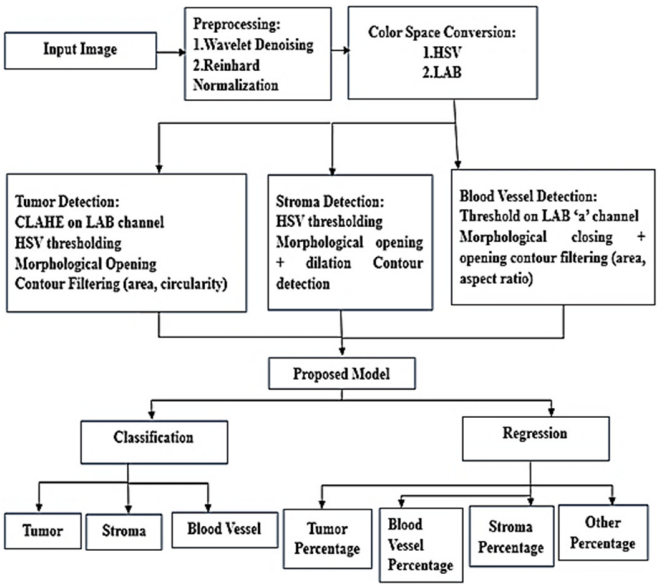


Fig. 1. Proposed architecture.

## III. IMPLEMENTATION

### A. Patch Extraction and Preprocessing

Each WSI is patch-divided, and RGB channels are separated into 100×100 matrices. The Red channel is split into 25 non-overlapping 2×2 blocks, each processed with Haar DWT and denoised using VisuShrink with a universal hard threshold. After inverse DWT, the absolute HH, HL, LH, and LL coefficients are extracted. The same procedure is applied to the Green and Blue channels, producing a denoised RGB patch. These refined patches are used to identify stroma, blood vessels, and tumors.

### B. Stroma Detection

As stroma plays a key role in endometrial cancer prognosis, accurately measuring its percentage in a patch is vital. The process involves denoising the RGB image, normalizing R, G, and B values to [0, 1], and then calculating HSV components—$C_{max}$ , $C_{min}$, and $\Delta$ ($C_{max}$–$C_{min}$). Hue (H), Saturation (S), and Value (V) are determined and converted to OpenCV scales.

$$H_{CV} = \frac{H}{2} \quad (1)$$

$$S = \begin{cases} 0, & if\ C_{max} = 0 \\ \frac{\Delta}{C_{max}}, & Otherwise \end{cases}$$

$$S_{CV} = S \times 255 \quad (2)$$

$$V = C_{max}, \qquad V_{cv} = V \times 255 \quad (3)$$

where $C_{max}$ is the maximum of (R,G,B), and $C_{min}$ is the minimum of (R,G,B). The threshold for stroma detection is: H: 0–180, S: 0–80, V: 200–255.

### C. Blood Vessel Detection

Blood vessel regions are identified by analyzing color information, specifically targeting the A channel in the LAB color space, which is sensitive to red/green hues—ideal for detecting red-colored blood vessels in stained tissues. RGB is normalized and converted to linear RGB and then to XYZ using:

1. Linear RGB→XYZ color space; Normalize XYZ to D65 white reference; XYZ→LAB color space:

$$f(t) = \begin{cases} t^{\frac{1}{3}} & t > \delta^3 \\ \frac{t}{3\delta^2} + \frac{4}{29} & Otherwise \end{cases} \quad (4)$$

$L^* = 116 \cdot f(y) - 16$ , $a^* = 500 \cdot (f(x) - f(y))$ , and $b^* = 200 \cdot (f(y) - f(z))$.

Then:

$$L = \left(\frac{L^*}{100}\right) \cdot 255, A = a^* + 128, B = b^* + 128 \quad (5)$$

where $x$, $y$, $z$ are normalized XYZ and $\delta$ is a threshold parameter.

2. Thresholding for blood vessel detection:

From the LAB channels (5), the A channel is used to detect red components:

$$\begin{cases} A > Threshold \Rightarrow 255\ (Blood\ Vessel\ Pixel) \\ else \Rightarrow 0 \end{cases}$$

Blood vessels typically stain in strong red shades (especially in H&E staining). The LAB color space separates chromatic content (A, B) from luminance (L). Red pixels have high $A^*$ values, thus, they are suitable for segmentation.

### D. Tumor Detection

This process involves converting denoised RGB to HSV (similar to stroma), and applying a tumor-specific HSV threshold: H: 150–161, S: 70–255, V:60–255.

### E. EfficientNet

EfficientNet models (B0B7) use compound scaling to balance depth ($\alpha$), width ($\beta$), and input resolution ($\gamma$), optimizing accuracy and efficiency. B0 is lightweight, and B7 offers higher accuracy at a higher computational cost. Beyond B7, models suffer from diminishing returns, overfitting, and

increased complexity. To overcome these issues, two enhancements are introduced:

3. $\delta$ factor: A new scaling dimension that regularizes deeper and wider networks, reducing overfitting.
4. Widthwise convolution layer: Enhances feature extraction across channels, boosting accuracy with minimal parameter overhead.

### *F. Proposed Method*

Compound scaling in EfficientNet jointly balances depth, width, and resolution using a global coefficient ($\phi$), unlike conventional methods that scale the dimensions independently. These additions extend traditional compound scaling, improving the trade-off between model complexity, performance, and generalization. In the proposed EfficientNet-B7.5ΔR, $\delta$ is a regularization factor to counteract the overfitting risk that arises when networks are scaled deeper and wider. This ensures improved generalization in medical imaging tasks. The model scaling is now formulated as:

$$\begin{cases} Depth = \alpha^{\phi} \\ Width = \beta^{\phi} \\ Resolution = \gamma^{\phi} \\ Regularization = \delta^{\phi} \end{cases} \quad (6)$$

where $\phi$ is the compound coefficient controlling overall scaling magnitude ($\phi$=7.5), $\alpha$, $\beta$, and $\gamma$ are scaling constants from the existing EfficientNet, and $\delta$ is the new regularizing factor to reduce overfitting.

#### *1) Compound Scaling Principle (Baseline from EfficientNet)*

Let $\phi = 7.5$, $\alpha = 1.2$, $\beta = 1.1$. Scaled depth and width are calculated as follows:

$$d_{7.5} = \lfloor \alpha^{7.5} \rfloor = \lfloor 1.2^{7.5} \rfloor = \lfloor 3.92 \rfloor = 3$$

$$w_{7.5} = \lfloor \beta^{7.5} \rfloor = \lfloor 1.1^{7.5} \rfloor = \lfloor 2.04 \rfloor = 2$$

Here, more layers and wider filters will allow a more expressive model without inefficient overscaling. This model performs six feature recalibration modules and a 4× initial filter width increase (starting from 32 filters).

#### *2) Feature Recalibration Module with Channel Attention Block and Widthwise Expansion*

This is the core building block of EfficientNet, with:

- Expansion: Expand input channels by a factor (e.g., 4×).
- Widthwise convolution: Efficient spatial feature extraction.

The feature recalibration module performs adaptive channel-wise recalibration using global context. The widthwise convolution layer enhances the cross-channel feature extraction, enabling the model to capture subtle differences between tissue types. The widthwise convolution layer is introduced to enhance the interaction among feature channels without increasing the number of parameters significantly, as given in (7-10). It is implemented as a $1 \times k$ grouped convolution, where $k$ denotes the kernel size applied horizontally across the feature map.

The residual connections add input back to output if shapes match, as given in (11, 12).

To reduce overfitting, the EfficientNet-B7.5ΔR model integrates regularization techniques absent in the original EfficientNet-B7. Mixup augments training by blending images and labels, enhancing generalization. Label smoothing softens targets to prevent overconfidence and improve robustness to label noise. The EfficientNet-B7.5ΔR model extends the compound scaling factor ($\phi$) to 7.5, allowing balanced increases in depth, width, and resolution while mitigating overfitting through proportional data scaling.

### *G. Model Pipeline (Proposed Method)*

Let $x \in R^{H \times W \times C}$ be the input image, where $H = 600$, $W = 600$, and channel $C = 3$ represent the height, width, and color channels of the input histopathological image patch.

#### *1) Compound Scaling ($\phi$,$\alpha$,$\beta$)*

A compound scaling method is applied to uniformly scale network depth $d$, width $w$, and resolution $r$ using a global coefficient $\phi$. The proposed model uses $\phi = 7.5$, $\alpha = 1.2$ (depth multiplier), and $\beta = 1.1$ (width multiplier).

$$d = \alpha^{\phi}, w = \beta^{\phi}$$

Hence, the model's depth and width scaling factors are computed as:

Depth scale: $d \approx \lfloor \alpha^{\phi} \rfloor$, Width scale: $w \approx \lfloor \beta^{\phi} \rfloor$.

#### *2) Modified Feature Recalibration Module*

Each feature recalibration block consists of:

*a) Expansion via* $1 \times 1$ *Convolution*

$$Z_1 = \sigma(BN(W_e * X)) \text{ where } W_e \in \mathbb{R}^{1 \times 1 \times C \times (e \cdot C)} \quad (7)$$

where $e$ is the expansion factor (e.g., 4), $*$ denotes convolution, $\sigma$ is the Swish activation, and BN is Batch Normalization.

*b) Depthwise Convolution*

$$Z_2 = \sigma\big(BN(W_d \odot Z_1)\big) \text{ where } W_d \in \mathbb{R}^{3 \times 3 \times (e \cdot C) \times 1} \quad (8)$$

*c) Widthwise Convolution*

$$Y_{i,j,k} = \sum_{m=1}^{M} X_{i,j,m} * W_{k,m} \quad (9)$$

where $X_{i,j,m}$ is the input feature map, $X_{i,j,m}$ is the widthwise convolution layer, and $Y_{i,j,k}$ is the resulting output feature map. This operation allows each channel to aggregate spatial information along the width dimension, improving contextual awareness and cross-channel communication within the recalibration block.

*d) Projection via 1×1 Convolution:*

$$Z_3 = BN(W_p * Z_2) \text{ where } W_p \in \mathbb{R}^{1 \times 1 \times (e.C) \times C'} \quad (10)$$

*e) Residual Connection*

Residual connections add identity shortcuts, preventing vanishing gradients, enabling stable training of deeper networks, and improving convergence. In this model, they were integrated into feature recalibration modules:

$$Y = \begin{cases} Z_3 + X & if\ stride\ =\ 1\ and\ C\ =\ C' \\ Z_3 & Otherwise \end{cases} \quad (11)$$

Each convolution uses a regularization factor with weight decay $\delta = 0.001$.

*f) Global Feature Aggregation*

$F = GAP(Y)$ where $GAP$ is Global Average Pooling.

$$F' = Dropout(0.5)(F)$$

$$F_{shared} = ReLU(W_f F^{|} + b_f) \text{ where } W_f \in \mathbb{R}^{512 \times d} \quad (12)$$

In these equations, $W_e$, $W_d$, and $W_p$ are weights for expansion, depthwise, and projection, respectively, and $X$ is the input tensor.

*3) Multi-Task Heads*

*a) Regression Branch*

$$R = W_r \cdot ReLU(W_{r1} F_{shared} + b_{r1}) + b_r, \text{ where } R \in \mathbb{R}^4 \quad (13)$$

$$\mathcal{L}_{reg} = \frac{1}{N} \sum_{i=1}^{N} ||R_i - \widehat{R}_i||_2^2$$

where $R_i$ is the ground truth regression vector, $\hat{R}_i$ is the predicted regression output, and $N$ is the number of samples.

*b) Classification Branch*

$$P = softmax(W_c \cdot ReLU(W_{c1} F_{shared} + b_{c1}) + b_c)$$

With label smoothing $\varepsilon = 0.1$, the classification loss is:

$$\mathcal{L}_{cls} = -\sum_{i=1}^{N} \sum_{j=1}^{C} y_{ij}^{smooth} \log P_{ij} \quad (14)$$

where $y_{ij}^{smooth} = (1 - \varepsilon) \cdot y_{ij} + \frac{\varepsilon}{C}$ (smooth target label), $P_{ij}$ is the predicted probability of class $j$, and $C$ is the number of classes.

*4) Total Loss Function*

The final loss function combines regression and classification (13, 14):

$$\mathcal{L}_{total} = \mathcal{L}_{reg} + \mathcal{L}_{cla} + \delta ||\theta||_2^2 \quad (15)$$

where $\delta = 0.001$, and $\Theta$ denotes all trainable parameters. Mixup smooths decision boundaries, reduces memorization, and enhances robustness under class imbalance and label noise, leading to improved generalization.

*H. Algorithm*

```
Algorithm 1: Regularization Strategy
  EfficientNet-B7.5ΔR
Input: Training data (X,Y), Compound
  scaling factor ϕ = 7.5
Output: Trained EfficientNet-B7.5ΔR model
For each training iteration do:
  Randomly select (x_i, y_i) and (x_j, y_j)
  Sample λ~Beta(a,a)
  x̃ ← λ*x_i+(1−λ)*x_j
  ỹ ← λ*y_i+(1−λ)*y_j
  use (x̃, ỹ) for training
End For
# Label Smoothing
For each label y in Y do:
  For each class k do:
    ŷ[k] ← (1 − ε)y[k] + ε/K
  End For
End For
Compute depth_scale ← α^ϕ
Compute width_scale ← β^ϕ
Compute resolution_scale ← γ^ϕ
Initialize EfficientNet-B7.5ΔR with scaled
parameters
For epoch = 1 to EPOCHS do
  Train model using Adam optimizer
  Update weights using total loss
  Monitor accuracy, R², and loss
End For
Return trained model
```

Figure 2 depicts blood vessel percentage per patch using A-channel thresholding in LAB color space to detect red-rich vascular regions in H&E-stained slides. Vessel content varies widely, from under 5% to over 25%, reflecting tissue heterogeneity. Figure 3 depicts tumor content across image patches from a histopathological WSI. The X-axis denotes patch indices, and the Y-axis indicates tumor pixel percentages. Tumor regions were segmented via HSV thresholding (H 150–161), capturing the pinkish-purple tones typical of tumors in H&E staining. Tumor presence ranges from ~30% to 75%, reflecting notable tissue heterogeneity. Figure 4 shows the stroma percentage per patch in a WSI. Using HSV thresholding (H: 0–180, S: 0–80, V: 200–255) to capture the bright, low-saturation signature of stroma in H&E-stained tissue, the stroma content varies from 10% to over 60%, indicating microenvironment heterogeneity.

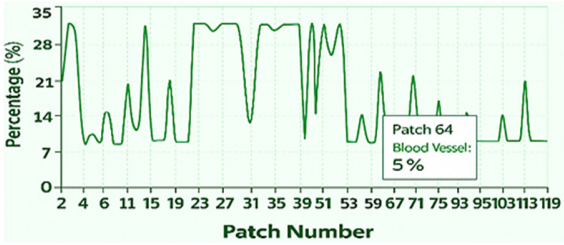


Fig. 2. Blood vessel content across histopathological patches.

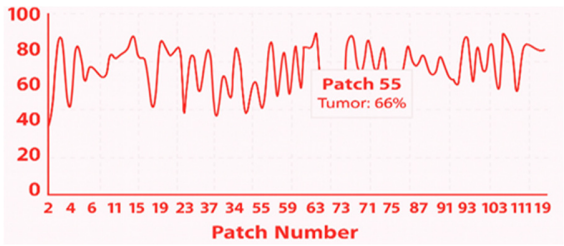


Fig. 3. Tumor content across histopathological patches.

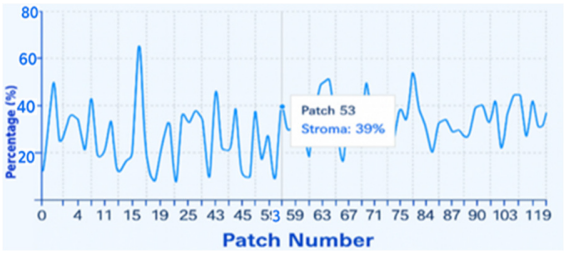


Fig. 4. Stroma content across histopathological patches.

Figure 5 shows that Accuracy, Precision, Recall, and F1-score improve rapidly and stabilize above 0.94 after epoch 5, with Precision peaking near 0.965—indicating balanced, well-generalized performance. The confusion matrix in Figure 6 was computed on a challenging held-out subset of 314 test patches, used for class-wise error analysis. Overall accuracy on this subset was ~90%. In Figure 7, total loss stabilizes after epoch 8, with low regression and decreasing classification loss, indicating effective learning. Figure 8 shows strong performance on tumor, vessel, and stroma detection, with an overall accuracy of ~96%.

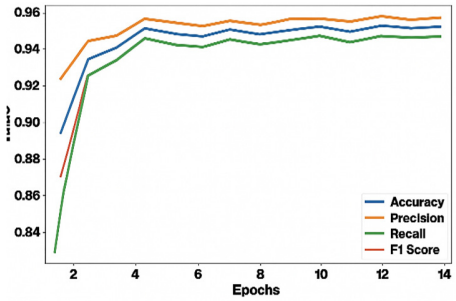


Fig. 5. Classification metrics across epochs.

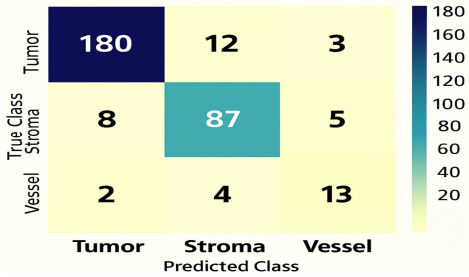


Fig. 6. Confusion matrix for tissue classification.

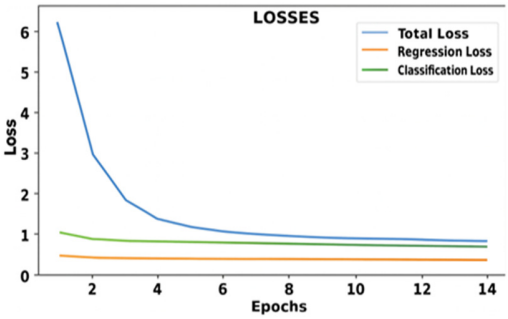


Fig. 7. Training losses over epochs.

| | Precision | Recall | f1-Score | Support |
|---|---|---|---|---|
| Tumor | 0.97 | 0.99 | 0.98 | 535 |
| Stroma | 0.86 | 1.00 | 0.92 | 18 |
| Vessel | 0.00 | 0.00 | 0.00 | 19 |
| Accuracy | | | 0.96 | 572 |
| Macro avg | 0.61 | 0.66 | 0.63 | 572 |
| Weighted avg | 0.93 | 0.93 | 0.95 | 572 |

Fig. 8. Classification report for tumor, stroma, and vessel segmentation.

Figures 9 and 10 illustrate the performance of the model. In Figure 9, the $R^2$ score improves from ~0.40 to >0.80 after epoch 5, indicating accurate regression and convergence. Figure 10 shows high AUCs for the classification of stroma (1.00), vessel (0.96), and tumor (0.95), highlighting the strong sensitivity and discriminative power of the model, especially for stroma.

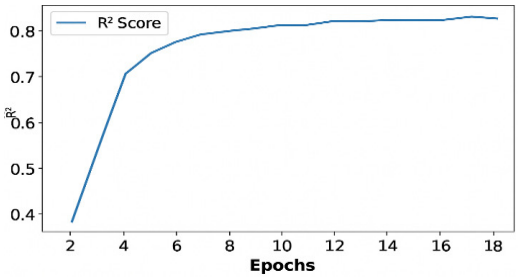


Fig. 9. $R^2$ progression across training epochs.

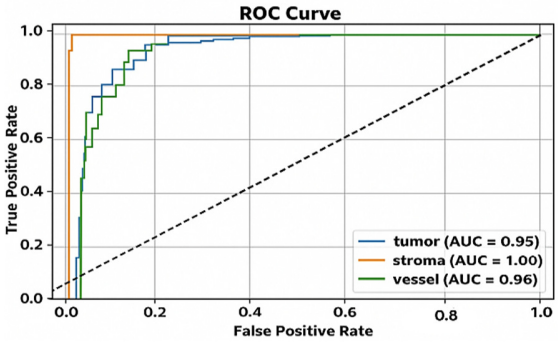


Fig. 10. ROC curves for tumor, stroma, and vessel classification.

## IV. COMPARATIVE ANALYSIS OF RESULTS

Tables I-VII compare the results of the proposed model with those of EfficientNet-B7, trained and validated on the same dataset under identical experimental conditions (same optimizer, batch size, and augmentation). The proposed EfficientNet-B7.5ΔR achieved 6% higher validation accuracy, while slightly underfitting in training suggests good regularization. The proposed model achieved a 12% higher $R^2$ on validation. The negative $R^2$ gap indicates better generalization than training fit, reflecting strong regularization. The lower classification loss on validation shows better convergence and less overfitting. Regression performance is also stronger, with a better validation fit. The proposed model achieves a 5% increase in validation F1-score and no spike in validation loss.

TABLE I. CLASSIFICATION ACCURACY COMPARISON

| Model | Final validation accuracy | Final training Accuracy | Accuracy gap |
|---|---|---|---|
| EfficientNet-B7 | 0.876 | 0.876 | 0.000 |
| EfficientNet-B7.5ΔR | 0.935 | 0.885 | 0.050 |

TABLE II. REGRESSION PERFORMANCE($R^2$ SCORE)

| Model | Final validation $R^2$ score | Final training $R^2$ score | $R^2$ gap |
|---|---|---|---|
| EfficientNet-B7 | 0.58 | 0.62 | -0.04 |
| EfficientNet-B7.5ΔR | 0.6938 | 0.6090 | -0.085 |

TABLE III. CLASSIFICATION LOSS

| Model | Final validation loss | Final training loss | Loss gap |
|---|---|---|---|
| EfficientNet-B7 | 0.57 | 0.57 | 0.00 |
| EfficientNet-B7.5ΔR | 0.4859 | 0.5453 | -0.0594 |

TABLE IV. REGRESSION LOSS

| Model | Final validation loss | Final training loss | Loss gap |
|---|---|---|---|
| EfficientNet-B7 | 0.031 | 0.034 | -0.003 |
| EfficientNet-B7.5ΔR | 0.0288 | 0.0345 | -0.0057 |

TABLE V. CLASSIFICATION F1 SCORE

| Model | Final training F1-score | Final validation F1-score |
|---|---|---|
| EfficientNet-B7 | 0.875 | 0.876 |
| EfficientNet-B7.5ΔR | 0.885 | 0.935 |

Table VI shows the performance of the proposed EfficientNet-B7.5ΔR model under 5-fold cross-validation. Reported values represent fold-wise metrics on validation sets. The model demonstrates consistent generalization performance across folds, confirming robustness. In general, the proposed EfficientNet-B7.5ΔR achieves 96% accuracy and AUC values of 0.95–1.00, outperforming existing models.

TABLE VI. 5 FOLD CROSS-VALIDATION PERFORMANCE

| Fold | Accuracy | Precision | Recall | F1-score |
|---|---|---|---|---|
| 1 | 95.8 | 95.4 | 95.6 | 95.5 |
| 2 | 96.5 | 96.2 | 96.1 | 96.2 |
| 3 | 96.2 | 96.0 | 96.3 | 96.1 |
| 4 | 96.0 | 96.9 | 96.1 | 96.0 |
| 5 | 96.1 | 96.3 | 95.9 | 96.1 |

TABLE VII. MODEL COMPLEXITY AND COMPUTATIONAL EFFICIENCY

| Model | Model size (MB) | FLOPs (G) | Inference time (ms/Patch) |
|---|---|---|---|
| EfficientNet-B7 | 159.2 | 5.3 | 31 |
| EfficientNet-B7.5ΔR | 142.4 | 4.1 | 24 |

## V. CONCLUSION

This study presented the EfficientNet-B7.5ΔR model for histopathological analysis of endometrial cancer. By integrating a $\delta$-regularization factor, widthwise convolution, and compound scaling ($\phi = 7.5$), the model achieves balanced depth, width, and resolution, improving generalization and minimizing overfitting. The proposed model exceeds the baseline EfficientNet-B7 with improvements of 6% in accuracy, 12% in $R^2$, and 5% in F1-score. The proposed model automatically estimates tumor, stroma, and vascular tissue proportions and computes key histological ratios (tumor-stroma, tumor-vessel, stroma-vessel) as prognostic markers. It generates an interpretable prognosis indicator with color-coded dashboards for quick clinical assessment. Future work will enhance vessel sensitivity through targeted augmentation, balanced sampling, and vascular biomarker integration.

## REFERENCES


[1] R. S. S. Anwar, "EfficientNet Algorithm for Classification of Different Types of Cancer," *Artificial Intelligence and Applications*, June 2023, https://doi.org/10.47852/bonviewAIA32021004.

[2] H. Van Thanh, N. D. Quang, T. M. Phuong, K. H. Jo, and V. D. Hoang, "A compact version of EfficientNet for skin disease diagnosis application," *Neurocomputing*, vol. 620, Mar. 2025, Art. no. 129166, https://doi.org/10.1016/j.neucom.2024.129166.

[3] R. Hong, W. Liu, D. DeLair, N. Razavian, and D. Fenyö, "Predicting endometrial cancer subtypes and molecular features from histopathology images using multi-resolution deep learning models," *Cell Reports Medicine*, vol. 2, no. 9, Sept. 2021, https://doi.org/10.1016/j.xcrm.2021.100400.

[4] M. Khened, A. Kori, H. Rajkumar, G. Krishnamurthi, and B. Srinivasan, "A generalized deep learning framework for whole-slide image segmentation and analysis," *Scientific Reports*, vol. 11, no. 1, June 2021, Art. no. 11579, https://doi.org/10.1038/s41598-021-90444-8.

[5] A. A. Patel, F. Ginhoux, and S. Yona, "Monocytes, macrophages, dendritic cells and neutrophils: an update on lifespan kinetics in health and disease," *Immunology*, vol. 163, no. 3, pp. 250–261, July 2021, https://doi.org/10.1111/imm.13320.

[6] L. Burrows, D. Sculthorpe, H. Zhang, O. Rehman, A. Mukherjee, and K. Chen, "Mathematical modelling and deep learning algorithms to automate assessment of single and digitally multiplexed immunohistochemical stains in tumoural stroma," *Journal of Pathology Informatics*, vol. 15, Dec. 2024, Art. no. 100351, https://doi.org/10.1016/j.jpi.2023.100351.

[7] M. W. Purbandanu, A. Kurniawan, R. Yanuarta, M. Munsarif, and A. A. Awoseyi, "EfficientNet for Medical Image Classification: Performance vs. Efficiency in Skin Cancer Detection," *Journal of Intelligent Computing & Health Informatics*, vol. 5, no. 2, pp. 43–50, Sept. 2024, https://doi.org/10.26714/jichi.v5i2.14338.

[8] M. Albertí-Valls, S. Olave, A. Olomí, A. Macià, and N. Eritja, "Advances in Immunotherapy for Endometrial Cancer: Insights into MMR Status and Tumor Microenvironment," *Cancers*, vol. 16, no. 23, Nov. 2024, Art. no. 3918, https://doi.org/10.3390/cancers16233918.

[9] D. Komura, M. Ochi, and S. Ishikawa, "Machine learning methods for histopathological image analysis: Updates in 2024," *Computational and Structural Biotechnology Journal*, vol. 27, pp. 383–400, 2025, https://doi.org/10.1016/j.csbj.2024.12.033.

[10] A. Alqhatani, T. K. S. R. Babu, T. R. Mahesh, S. B. Khan, O. Saidani, and M. T. Quasim, "Automated classification and explainable AI analysis of lung cancer stages using EfficientNet and gradient-weighted class activation mapping," *Frontiers in Medicine*, vol. 12, Sept. 2025, Art. no. 1625183, https://doi.org/10.3389/fmed.2025.1625183.

[11] M. Tan and Q. V. Le, "EfficientNet: Rethinking Model Scaling for Convolutional Neural Networks." arXiv, Sept. 11, 2020, https://doi.org/10.48550/arXiv.1905.11946.

[12] M. Tan and Q. V. Le, "EfficientNetV2: Smaller Models and Faster Training." arXiv, June 23, 2021, https://doi.org/10.48550/arXiv.2104.00298.

[13] A. Dosovitskiy *et al.*, "An Image is Worth 16x16 Words: Transformers for Image Recognition at Scale." arXiv, June 03, 2021, https://doi.org/10.48550/arXiv.2010.11929.

[14] R. Wang, Q. Li, G. Shi, Q. Li, and D. Zhong, "A deep learning framework for predicting endometrial cancer from cytopathologic

images with different staining styles," *PLOS ONE*, vol. 19, no. 7, 2024, Art. no. e0306549, https://doi.org/10.1371/journal.pone.0306549.

[15] K. He, X. Zhang, S. Ren, and J. Sun, "Deep Residual Learning for Image Recognition." arXiv, Dec. 10, 2015, https://doi.org/10.48550/arXiv.1512.03385.

[16] C. Szegedy, S. Ioffe, V. Vanhoucke, and A. Alemi, "Inception-v4, Inception-ResNet and the Impact of Residual Connections on Learning." arXiv, Aug. 23, 2016, https://doi.org/10.48550/arXiv.1602.07261.

[17] J. Howard and S. Gugger, "fastai: A Layered API for Deep Learning," *Information*, vol. 11, no. 2, Feb. 2020, Art. no. 108, https://doi.org/10.3390/info11020108.

[18] B. R. Corr, B. K. Erickson, E. L. Barber, C. M. Fisher, and B. Slomovitz, "Advances in the management of endometrial cancer," *BMJ*, vol. 388, Mar. 2025, Art. no. e080978, https://doi.org/10.1136/bmj-2024-080978.

[19] V. Makker *et al.*, "Endometrial cancer," *Nature Reviews Disease Primers*, vol. 7, no. 1, Dec. 2021, Art. no. 88, https://doi.org/10.1038/s41572-021-00324-8.

[20] X. Zhu, J. Ying, H. Yang, L. Fu, B. Li, and B. Jiang, "Detection of deep myometrial invasion in endometrial cancer MR imaging based on multi-feature fusion and probabilistic support vector machine ensemble," *Computers in Biology and Medicine*, vol. 134, July 2021, Art. no. 104487, https://doi.org/10.1016/j.compbiomed.2021.104487.

[21] T. Brázdil, M. Gallo, R. Nenutil, A. Kubanda, M. Toufar, and P. Holub, "Automated annotations of epithelial cells and stroma in hematoxylin–eosin-stained whole-slide images using cytokeratin re-staining," *The Journal of Pathology: Clinical Research*, vol. 8, no. 2, pp. 129–142, 2022, https://doi.org/10.1002/cjp2.249.

[22] Y. Feng *et al.*, "Spatially organized tumor-stroma boundary determines the efficacy of immunotherapy in colorectal cancer patients," *Nature Communications*, vol. 15, no. 1, Nov. 2024, Art. no. 10259, https://doi.org/10.1038/s41467-024-54710-3.

[23] C. Zhang *et al.*, "HIFUNet: Multi-Class Segmentation of Uterine Regions From MR Images Using Global Convolutional Networks for HIFU Surgery Planning," *IEEE Transactions on Medical Imaging*, vol. 39, no. 11, pp. 3309–3320, Aug. 2020, https://doi.org/10.1109/TMI.2020.2991266.

[24] D. M. Koh *et al.*, "Artificial intelligence and machine learning in cancer imaging," *Communications Medicine*, vol. 2, no. 1, Oct. 2022, Art. no. 133, https://doi.org/10.1038/s43856-022-00199-0.

[25] C. W. Wang *et al.*, "Deep learning to assess microsatellite instability directly from histopathological whole slide images in endometrial cancer," *npj Digital Medicine*, vol. 7, no. 1, May 2024, Art. no. 143, https://doi.org/10.1038/s41746-024-01131-7.

[26] O. Al-Omari, O. Alkhatib, and T. Al-Omari, "CNN-Based Automated Detection of Metastatic Cancer in Histopathology Images," *Engineering, Technology & Applied Science Research*, vol. 15, no. 4, pp. 24478–24485, Aug. 2025, https://doi.org/10.48084/etasr.10888.

[27] T. Gelton, S. Vermorgen, and F. Ciompi, "Endometrium Carcinoma Pipelle biopsies." Zenodo, Aug. 23, 2022, https://doi.org/10.5281/zenodo.7372187.